Stereoscopic imaging of air showers with the first two HEGRA Cherenkov telescopes

A. Kohnle [a], F. Aharonian [a], A. Akhperjanian [b], S. Bradbury [d], A. Daum [a], T. Deckers [f],
J. Fernandez [c,d], V. Fonseca [c], M. Hemberger [a], G. Hermann [a], M. Heß [a], A. Heusler [a],
W. Hofmann [a], R. Kankanian [a,b], C. Köhler [a], A. Konopelko [a,e,1], E. Lorenz [d],
R. Mirzoyan [c,d], N. Müller [f], M. Panter [a], D. Petry [d], A. Plyasheshnikov [a,b], G. Rauterberg [f],
M. Samorski [f], W. Stamm [f], M. Ulrich [a], H.J. Völk [a], C.A. Wiedner [a], H. Wirth [a]

[a] *Max-Planck-Institut für Kernphysik, P.O. Box 103980, 69029 Heidelberg, Germany*
[b] *Yerevan Physics Institute, Alikhanian Br. 2, 375036 Yerevan, Armenia*
[c] *Universidad Complutense, Facultad Ciencias Fisicas, 28040 Madrid, Spain*
[d] *Max-Planck-Institut für Physik, 80805 München, Germany*
[e] *Altai State University, Barnaul, Russia*
[f] *Universität Kiel, Institut für Reine und Angewandte Kernphysik, 24118 Kiel, Germany*

Received 27 November 1995; revised manuscript received 22 January 1996

Abstract

With systems of atmospheric Cherenkov telescopes, providing stereo images of air showers, the shower parameters, such as the direction, core location, and height of shower maximum can be determined event by event. Techniques for the reconstruction of air showers are introduced, and are demonstrated using data from the first two HEGRA Cherenkov telescopes. Applied to observations of the Crab nebula, a clear signal is observed; the angular distribution of the excess events is consistent with Monte Carlo simulations of the expected resolution.

1. Introduction

At the site of the HEGRA air shower experiment on the Roque de los Muchachos on the Canarian Island of La Palma, a system of five Imaging Atmospheric Cherenkov Telescopes is currently under construction. In 1994, two telescopes were operational: a smaller prototype telescope and the first unit of the future system, albeit not with the final camera. The distance of these two telescopes of 92.5 m made stereoscopic imaging of cosmic ray showers possible, with show-

ers being observed in coincidence in both telescopes. Stereoscopic imaging permits a full reconstruction of the shower axis, namely of the shower direction and the shower core position. In this paper, we describe the analysis of coincident events, their characteristics, and their interpretation in terms of simple geometrical pictures.

2. The HEGRA Cherenkov telescopes

In spite of continuous hardware changes to improve their performance, the HEGRA Cherenkov telescopes

---

[1] On leave from Altai State University, Barnaul, Russia.

Table 1
Characteristics of the HEGRA Cherenkov telescopes

	CT1	CT2
Mount		
Type	equatorial	alt-azimuth
Mirrors		
Total number	18	30
Shape	spherical	spherical
Diameter	60 cm	60 cm
Focal length	492 ± 4 cm	492 ± 4 cm
Reflectivity (at 300 nm)	84%	84%
Total area	5 m^2	8.5 m^2
Camera		
Photomultiplier	type FEU-130	type FEU-130
Quantum efficiency (at 375 nm)	19%	19%
Pixel size	36 mm (0.43°)	36 mm (0.43°)
Number of pixels	37	61
Field of view	3.0°	3.9°

(CT's) are described here as they were operational during 1994, when the data for the subsequent analysis were taken. The first telescope (from hereon referred to as CT1) has been presented in detail [1], so only a brief description will be given here. The properties of both telescopes are listed in Table 1. CT1 has an equatorial mount and a 5 m^2 reflector dish consisting of 18 spherical glass mirrors with 60 cm diameter each and a focal length of 492 ± 4 cm. The second, larger telescope (CT2) is alt-azimuth mounted with an 8.5 m^2 reflector consisting of 30 mirrors. The angular resolution of the single mirrors is 20–40″, the typical reflectivity is 84% at $\lambda = 300$ nm, increasing to 89% at $\lambda > 420$ nm. The cameras consist of 37 (CT1) and 61 (CT2) 12-stage Soviet FEU-130 photomultiplier tubes (PMTs) with 25 mm photocathode diameter, arranged in a hexagonal array. To avoid dead space between the photocathodes, UV-transparent Plexiglas light concentrators are placed in front of the PMTs; they have the shape of truncated cones with hexagonal entrance faces 36 mm across. Each PMT then views 0.43° of the sky. CT2 is equipped with an anticoincidence shield for muon rejection consisting of a 20 mm thick NE104 scintillator cylinder and cover plate read out by 5 PMTs.

The telescopes are driven by stepping motors with a reduction gear using pulses from frequency synthesizers. The step size is equivalent to 0.02° rotation;

positions are measured with 14-bit Gray coded shaft encoders.

The readout system for both telescopes uses standard NIM and CAMAC modules; the CAMAC crates are interfaced to MAC II computers. The AC-components of the signals from each PMT are amplified by a factor of 10 (CT1) or 28 (CT2) and then sent to pulse height discriminators with a threshold corresponding to about 30 photoelectrons and to 10-bit charge-integrating ADCs (LeCroy 2249A). The discriminator outputs provide 7 ns pulses. These are fanned out to a majority unit which triggers the readout of the ADCs, shaft encoders, timing information, etc., if 2 out of 37 (CT1) or 2 out of 61 (CT2) pixels are above the threshold. Microsecond timing information comes from a Rb-clock that is calibrated automatically via GPS; its 5 MHz and 1 Hz clock signals are sent to a latch register. The anode currents of the PMTs are monitored using LeCroy 2232A ADCs, and the counting rates of the individual pixels are measured with LeCroy 4434 scalers.

3. Stereoscopic reconstruction of the shower axis

With two or more images of the same shower, a 3-dimensional reconstruction of the shower axis becomes possible. It is favorable to use a coordinate sys-

tem in which the orientation of the telescope dish and of the camera is fixed (see Fig. 1(a)). The xy-plane coincides with the camera plane. The z-axis points along the telescope axis. The x-axis projected onto the horizontal plane points along the line intersecting the telescopes, directed from CT1 to CT2. The origin is placed in the center of the camera of CT1. We assume that both cameras point in exactly the same direction; deviations are corrected by shifting the origin of the coordinate system of the camera images, as will be discussed later. The shower axis is characterized by a direction and a core position. One defines the shower core position $R = (x_{core}, y_{core})$ as the vector from the camera position to the point where the shower axis intersects the xy-plane. The shower angle θ is the angle between the shower and the telescope axis, with projections θ_x and θ_y on the xz- and yz-planes[2].

Fig. 1(b) illustrates how the shower angle θ is determined: the single camera images are shown here as the ellipses calculated using the Hillas parameters [2]. In the absence of fluctuations in the shower evolution and the imaging process, the shower axis is imaged onto a line coinciding with the major axis of the image. Both the image of the source as well as the point where the shower axis intersects the camera plane lie on this line. As a result, the shower direction can be determined by superimposing the images of the two cameras and intersecting the lines passing through the long axes of the ellipses, resulting in the intersection point $(-f\theta_x, -f\theta_y)$. Here, f denotes the focal length; the signs account for the mirror reflection. The angular resolution of the two-telescope system is governed by shower fluctuations and photon statistics, which cause measurement errors in the determination of image centers and of the image orientation; in particular, the resolution is poor if the two image axes are approximately collinear.

The shower core position is determined using a similar technique. The lines passing through the long axes of the ellipses are intersected, starting from the positions of the telescopes (Fig. 1(c)). Strictly speaking, this method is only valid if the telescopes look to the zenith; otherwise, the image planes are separated by a distance d_{12} along the telescope axes (see
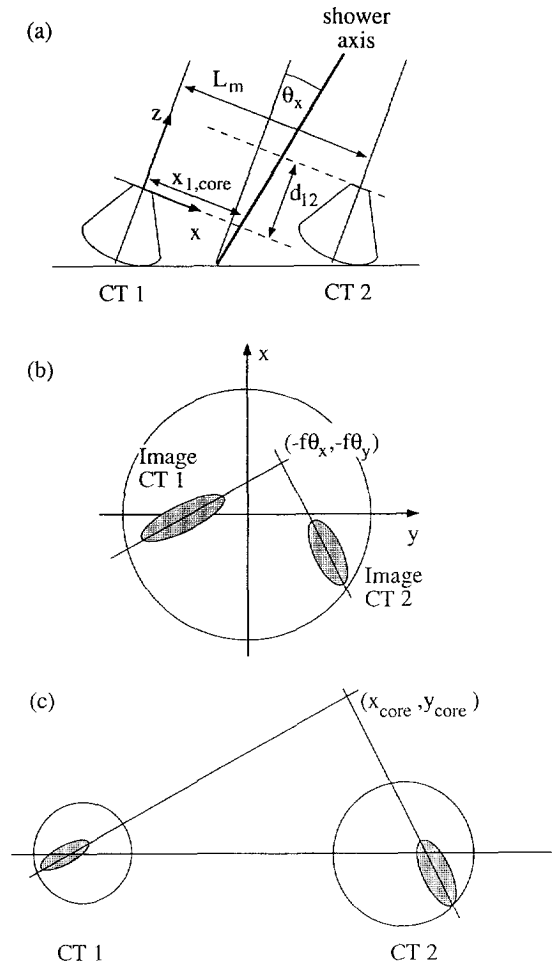

Fig. 1. (a) Definition of the geometry and the coordinate system: the xy-plane denotes the camera plane, z is oriented along the telescope axis, and the x-axis projected into the horizontal plane coincides with the line connecting the telescopes. L_m is the telescope distance along the x-axis, d_{12} the distance of the image planes along the z-axis, and θ_x the x-projection of the shower angle. $x_{1,core}$ is the x-projected shower core distance in the plane of the first telescope. (b) Reconstruction of the shower angle: The camera images are superimposed and the lines determined by the major axes of the ellipses are intersected. The intersection point has to be mirrored with respect to the camera center to determine the shower angle. (c) Reconstruction of the shower core: The lines determined by the major axes of the ellipses are intersected, starting from the positions of the telescopes (after correction for the distance d_{12} of the image planes, see text).

---

[2] Since the angles between triggered showers and the telescope axis are minimal, the small-angle approximation $\sin \theta_{x,y} \approx \tan \theta_{x,y} \approx \theta_{x,y}$ is used throughout the paper.

Fig. 1(a)), and a small displacement $(d_{12}\theta_x, d_{12}\theta_y)$ of the shower core location of CT2 has to be taken into account, when carrying out the reconstruction in the image plane of CT1.

4. Event selection and image processing

As the data acquisition systems of the two telescopes are independent, the coincident events were extracted in the software analysis, using the timing information from the Rb-clock that is read out with each event. Approximately 70% of CT1 events and 30% of CT2 events were coincident within 1 μs, with the coincidence rate being roughly 0.8 Hz at small zenith angles. Given the sub-microsecond time resolution, the rate of random coincidences is completely negligible. The data set used for the analysis presented here comprises about 120000 coincident events from observations of several objects, including the Crab nebula, taken in summer and fall of 1994.

Before combining data from the two telescopes, it is necessary to correct for misalignments of the telescope axes. Such misalignments can be caused either by imperfections of the tracking system or by deflections of the camera from its nominal position. Misalignment corrections can be determined by so-called point runs [3,1], where a bright star ($m_v \leq +3.0$) is scanned across the camera. With (ra, δ) denoting the right ascension and declination of the star, the telescopes are successively pointed to points in a lattice defined by

$$\left(ra \pm s\frac{i}{n_x}, \quad \frac{\delta \pm sj/n_y}{\cos \delta} \right),$$
$$0 \leq i \leq n_x, \quad 0 \leq j \leq n_y$$

where the hour angle of each point is calculated using the current sidereal time. At each position, all PMT currents are measured. For a typical point run, $s = 0.43°$ (the size of a pixel in the camera), and $n_x = n_y = 11$ (the lattice has 121 points).

From the point runs, contour plots of the current of each camera pixel can be made which contain information about point spread functions and pointing inaccuracies (Fig. 2).

A correction curve for the camera misalignment is constructed from point runs for various hour angles using a star whose declination is similar to the ob-
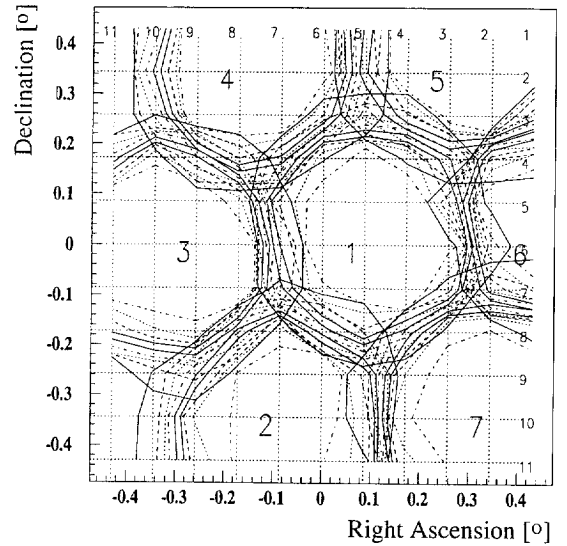

Fig. 2. A contour plot of the currents of the central pixels extracted using point run information. The x- and y-coordinates correspond to right ascension and declination relative to a bright star. The contour lines are equidistant, in steps of 10% of the maximum current of the central pixel. The deviation of the central pixel (pixel 1) from (0,0) represents the misalignment of the telescope axis. The steepness of the transition at the pixel borders, i.e., the spacing of contour lines, is a measure of the point spread function [3,1]. The contours trace the hexagonal aperture of the pixels.

served source. Correction curves for CT1 for various declinations are shown in Fig. 3. The observed pointing error is less than 0.2 degrees, corresponding to a maximal offset of the camera center by 1.7 cm. This pointing error is corrected by shifting the origins of the camera images.

To determine the image parameters, the pedestals, determined by artificially triggering the event read-out, are subtracted from each pixel. For noise suppression, only a subset of the pixels is used to calculate the image parameters [4]. A pixel is included in the image calculation if its signal is larger than 5 σ_i, or if it is larger than 3 σ_i and a neighboring pixel is part of the image. Here, σ_i is the pedestal fluctuation. All pixels not fulfilling these criteria are set to zero. Only events with 3 or more picture pixels in each camera are used. Afterwards, the orientation-dependent parameters are rotated into the common coordinate system. As CT1 is equatorially mounted and CT2 alt-azimuth mounted, there is a rotation of the field of view in CT2 which must be accounted for.
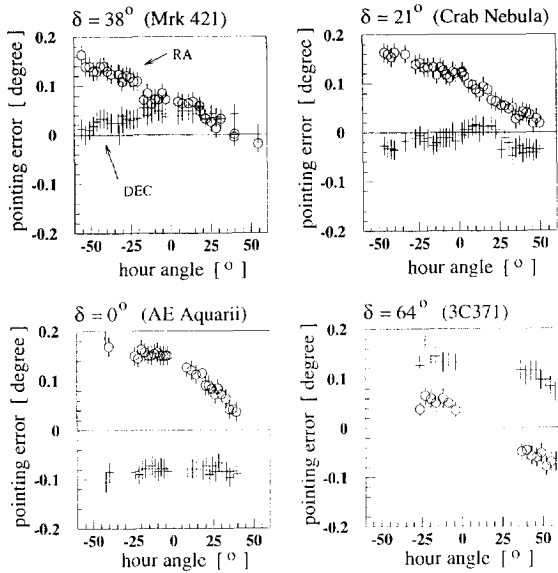
Fig. 3. Misalignment correction curves for CT1 for declination (crosses) and right ascension (open circles) as a function of hour angle. Camera misalignment was studied with several bright stars close to potential TeV γ-ray sources (indicated on top), at different declination angles.
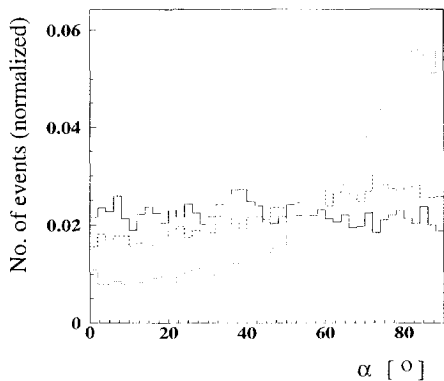

Fig. 4. Distribution in the orientation angle α of images in CT2, for events with a distance of the image center from the camera center between 0.6° and 0.7° (full line), between 1.1° and 1.2° (dashed), and for values > 1.2° (dotted). Images with $\alpha = 0$ point to the center of the camera, images with $\alpha = 90°$ point along the periphery.

A limiting factor for the following stereoscopic reconstruction is the small field of view, especially of the camera of CT1. Image parameters, in particular the orientation α of the image (i.e., the direction of its major axis) – crucial for the reconstruction proce-

dure – start to 'feel' the edge of the camera already for events with their image centers around 0.8° (CT1) and 1.1° (CT2) from the center of the camera; events beyond 0.9° (CT1) and 1.2° (CT2) are severely biased. This is most easily seen in distributions of the orientation of images at different points in the camera (Fig. 4). For events within the limit given above, the α-distribution is essentially uniform; events beyond point dominantly along the periphery of the camera ($\alpha = 90°$). Similar problems are observed in the measurement of the width and length of images. A general conclusion is that cameras of IACT systems should be designed to provide a margin of at least 0.7° to 0.8° between the outmost location of interesting images, and the edge of the camera. In the present analysis, however, no cuts on the distance of images to the camera edge were applied, since with the prototype cameras, such cuts would drastically limit the statistics. Parts of the analysis were repeated with a restricted sample, and showed a clear improvement in the resolution.

5. Correlation of the image centers and the shower height

In the following sections, the extraction of shower information from the two images is discussed. In order to completely reconstruct the shower axis in space, one has to make use of the information both concerning the location of the images within the cameras, and concerning their angular orientation. As a first step, however, it is useful to concentrate only on the location of images, as described by their centers of gravity.
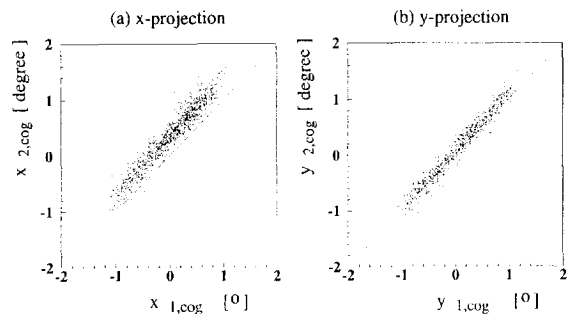

Fig. 5. The x (a) and y (b) projections of the image centers of the first telescope vs. the second telescope, plotted using events with zenith angles between 35 and 45 degrees. $y_{1,\text{cog}}$ denotes the y-projection of the image center of the first telescope, etc.

Images in the Cameras

CT 1   CT 2

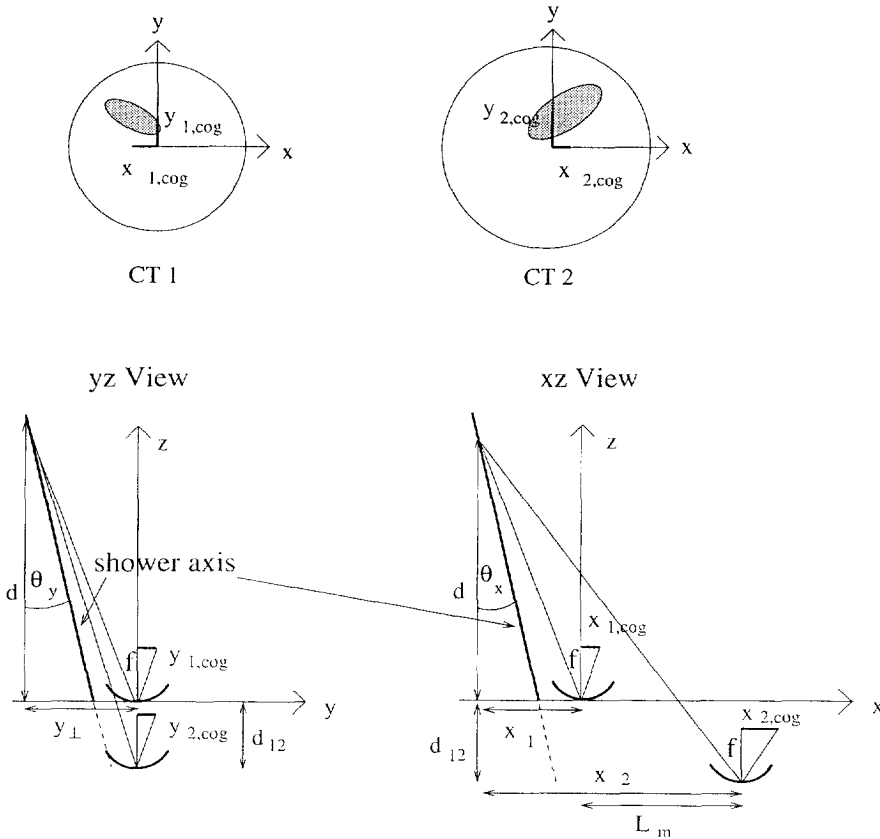yz View   xz View

Fig. 6. A simple model to explain the image center correlations; geometry not drawn to scale.

After rotating the images into the common coordinate system, one observes a strong correlation between the coordinates[3] of the images in the two cameras (Fig. 5). In the y-direction, i.e., perpendicular to the line joining the two telescopes (Fig. 1(a)), the two images tend to coincide (Fig. 5(b)). In the x-direction, along this line, the image in CT2 is shifted compared to the image in CT1 (Fig. 5(a)). Comparison of data from different zenith angular regions shows that the shift varies with zenith angle.

These correlations can be explained in a simple model, assuming that the location of the image center of gravity is determined by light emitted near the shower maximum, at a distance d from the cameras

(Fig. 6). In the yz-plane, the telescopes have the same position $y = 0$, in z they are offset by d_{12}. The shower maximum is located at a distance d, displaced by a distance $y_\perp$ from the telescope axes. Light coming from shower maximum is imaged to the positions $y_{1,cog}$ and $y_{2,cog}$ in the camera. From Fig. 6 follows:

$$\frac{y_{1,cog}}{f} = -\frac{y_\perp}{d}, \qquad \frac{y_{2,cog}}{f} = -\frac{y_\perp}{d + d_{12}}$$

with f as the focal length. Typically, d_{12} varies between 0 and 20 m, and is very small compared to the distance to the shower maximum, which ranges between 6 and 10 km. One sees that

$$y_{2,cog} - y_{1,cog} \approx 0$$

up to terms of order 10^{-3}. Therefore, the y-projections of the image centers should be identical, except for

---

[3] Here and in the following figures, image coordinates are usually given in degrees, using the focal length f as a conversion factor.
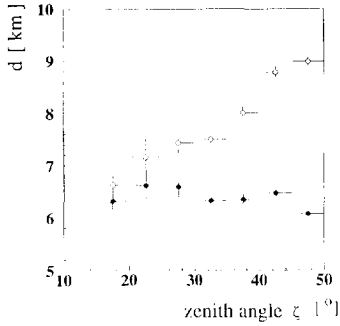
Fig. 7. The distance $\bar{d}$ (open circles) and height $\bar{h} = \bar{d}\cos\zeta$ (filled squares) of the shower maximum, determined using the image center correlations, plotted as a function of zenith angle ζ. Distances and heights refer to the La Palma site (2200 asl).

Fig. 8. The distribution of image centers in the camera, plotted separately for each telescope. $x_{1,\text{cog}}$ is the x-projection of the image center of the first telescope, etc.

fluctuations caused by photon statistics, effects of the granularity of the camera, etc.

In the xz-plane, the telescope positions are offset by L_m along x and d_{12} along z (L_m is the telescope distance projected into the camera plane). Light from a distance d arrives at somewhat different angles at the two telescopes. From Fig. 6 one obtains

$$\frac{x_{1,\text{cog}}}{f} = -\frac{x_1}{d},$$
$$\frac{x_{2,\text{cog}}}{f} = -\frac{x_2}{d + d_{12}} = -\frac{x_1 - L_m}{d + d_{12}}$$

so that, again using $d_{12} \ll d$,

$$x_{2,\text{cog}} - x_{1,\text{cog}} = \frac{fL_m}{d}$$

Hence, the x-projections are offset by an amount that depends on the distance of the shower emission maximum d. With f and L_m known, one can use the average offset $x_{2,\text{cog}} - x_{1,\text{cog}}$ to determine the average distance $\bar{d}$ to the shower maximum (or, to be more precise, the average of $1/d$).

Dividing the events into zenith angle bins, one can extract the zenith angle dependence of the mean distance $\bar{d}$ as well as the projection of this distance into the vertical, $\bar{h} = \bar{d}\cos\zeta$ (Fig. 7). In the crude model used here, $\bar{h}$ would be the height of the shower maximum. In reality, the mapping between distance along the shower axis and location along the image axis is nonlinear, and is also smeared due to the transverse size of the shower, meaning that the effective height determined from the image centers will not exactly coincide with the height of maximum emission. Nev-
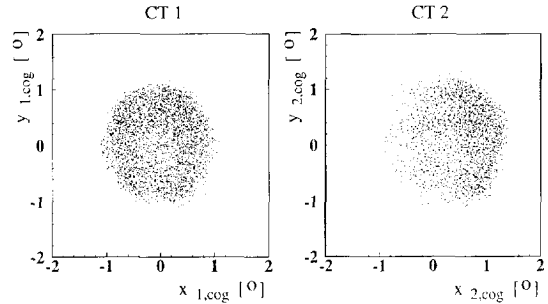
ertheless, the height $\bar{h}$ determined with this technique, $\bar{h} \approx$ 6–7 km above La Palma, or 8 to 9 km above sea level, is consistent with the height of the shower maximum, as predicted by Monte Carlo simulations. One might expect $\bar{h}$ to increase with increasing zenith angle, due to the longer path length through the atmosphere. The observation that, in Fig. 7, $\bar{h}$ is essentially independent of zenith angle can be attributed to an increase of trigger threshold with increasing zenith angle, resulting in a deeper penetration [5].

The width of the distribution $y_{1,\text{cog}} - y_{2,\text{cog}}$ provides a direct measure for the precision with which the image centers are determined. These issues will be addressed in more detail later in Section 8 of this paper.

One can also look at the distribution of image centers in the camera for each telescope separately (Fig. 8). The distribution of image centers in CT1 is more or less homogeneous, whereas in CT2 there is a predominance of image centers on the side of the camera pointing away from CT1. An explanation will discussed below, in the context of the reconstruction of the shower direction and of the core location (see Section 6).

6. Reconstructed shower directions and core locations

As a next step, the reconstruction of the shower direction and of the core location is discussed, using the location and orientation of both images. As discussed above, the shower angle θ (between the shower and the telescope axes) is derived by intersecting the center lines of the superimposed images. Fig. 9 shows the
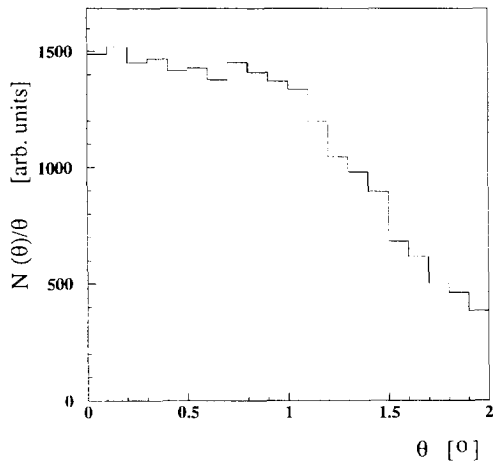
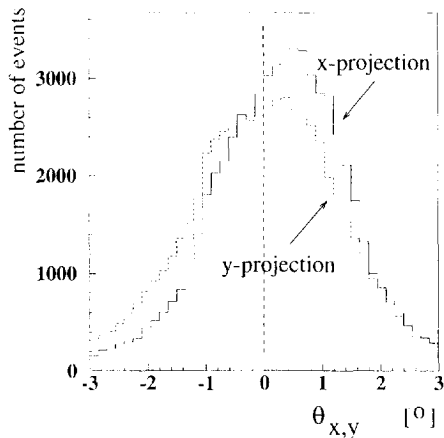Fig. 9. The distribution in detected shower angles, $N(\theta)/\theta$.

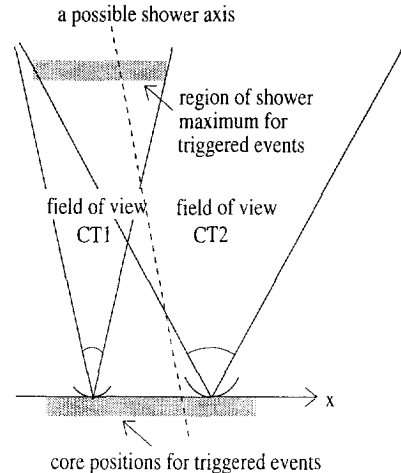Fig. 10. The distribution in projected shower angles, for the x and y projections.

Fig. 11. An illustration of the origin of the asymmetry in the distributions of shower angles and image centers. The shower maximum has to lie in the field of view of both telescopes, and the telescope locations have to be within the Cherenkov light pool. The figure is not drawn to scale.

distribution in θ. For small θ, the solid angle associated with a θ-interval increases linearly with θ; this trivial dependence is removed in Fig. 9 by plotting $N(\theta)/\theta$. The resulting distribution is flat out to about 1.1 degrees and then falls off rapidly. The radius of the field of view of the smaller CT1 is 1.5 degrees, but the trigger efficiency drops close to the edge of the camera, since a significant fraction of light is imaged beyond the camera edge.

The y-projection of shower angles is symmetric while the x-projection is somewhat asymmetric (Fig. 10). This together with the asymmetric distribution of image centers in CT2 (Fig. 8) can be explained. In order to trigger both telescopes, two

conditions must be met:

(1) the shower maximum must be in the field of view of both telescopes;

(2) both telescopes must be within the Cherenkov light radius of about 120 m on the ground.

This is illustrated schematically in Fig. 11. Allowed (triggered) shower axes penetrate both shaded areas. The larger field of view of CT2 thus leads to showers preferentially inclined towards CT2, and to showers having image centers preferentially on the side of the camera of CT2 pointing away from CT1.

Core positions are reconstructed by intersecting the image center lines emanating from the telescope locations (Fig. 1(c)). The distribution of reconstructed shower core positions is shown in Figs. 12(a) and 13. Evident is a strong concentration of shower cores within a radius of about 20 m around each telescope and a deficit of shower cores along the x-axis on the far side of each telescope. However, these characteristics do not mirror the true shower core distribution; they are an unavoidable artefact of the reconstruction technique. Whenever a shower core is located near $y = 0$, the two image center lines intersect at very small angles, resulting in large errors in the reconstructed core location. In the presence of measurement errors, the transformation from measured orientations to reconstructed positions tends to map those shower cores
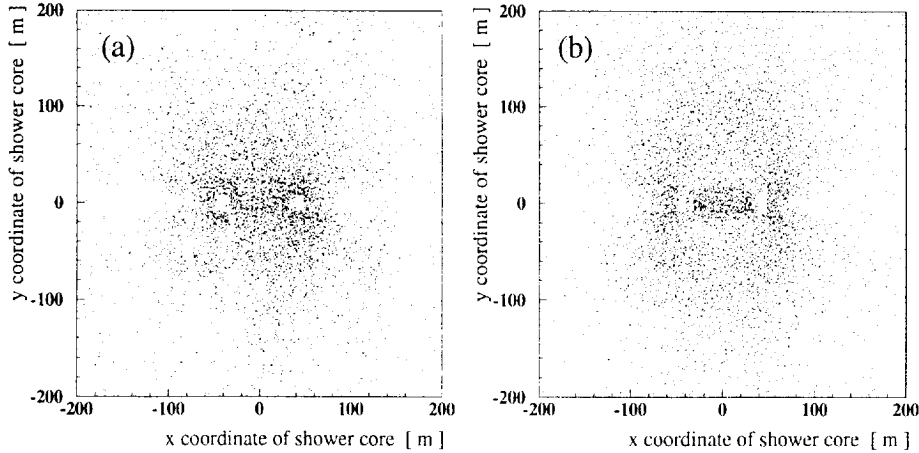
Fig. 12. (a) The distribution of shower cores in the image plane of CT1. The telescopes are located symmetrically at (−46.25,0) m and (46.25,0) m. (Due to the variation in zenith angles, the separation of the telescopes is not constant, when projected onto the image plane. For this plot, this effect has been removed by a minor rescaling of the x-axis such as to yield a constant separation.) Points within 10 m of the telescopes are excluded, in order not to saturate the dynamic range of the plot. (b) The result of a simple simulation of the effect of measurement errors, see text.
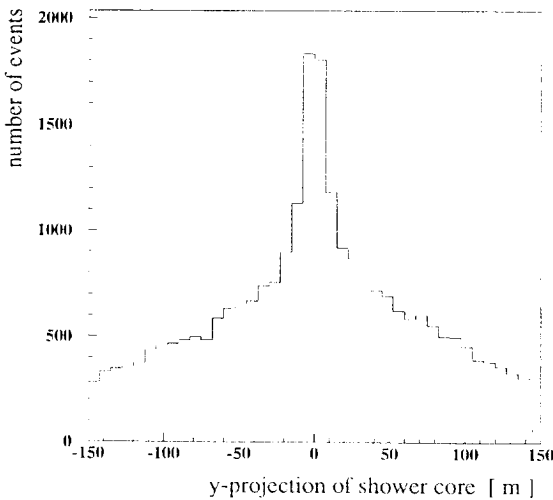

Fig. 13. The y-projection of shower core positions in the plane of CT1. The position of the telescope is at $y = 0$.

preferentially into the vicinity of the telescopes. This feature is illustrated by a simple Monte Carlo simulation which generates a homogeneous distribution of shower cores. For each random shower core position, the direction to both telescopes is calculated. To simulate the directional resolution of the single images, these directions are then smeared with a gaussian distribution with a width of 12° (for the typical resolu-

tion in α, see below), and a 'reconstructed' core position is calculated. The resulting core distribution is shown in Fig. 12(b); the simulation reproduces the gross characteristics of the shower core distribution in the data.

For the future system of five telescopes, this distortion in the reconstruction of core positions will of course be drastically reduced for events viewed by three or more non-collinear telescopes.

With the two trigger requirements described above, one expects pronounced correlations between the directions and the core positions for triggered events. Fig. 14 illustrates that in the yz-plane, the possible angles θ_y for a shower with core location y_{core} lie between ϕ_1 and ϕ_2, or

$$\frac{y_{core} - d\theta_{fov}/2}{d} \leq \theta_y \leq \frac{y_{core} + d\theta_{fov}/2}{d},$$

with $\theta_{fov} \approx 3°$ as the full field of view of the smaller telescope and d as the distance to the shower maximum. Fig. 15 shows the y-projected shower core vs. the y-projected shower angle. Indeed, a correlation is observed, which is well described by the expression given above, with $d \approx 7$ km.
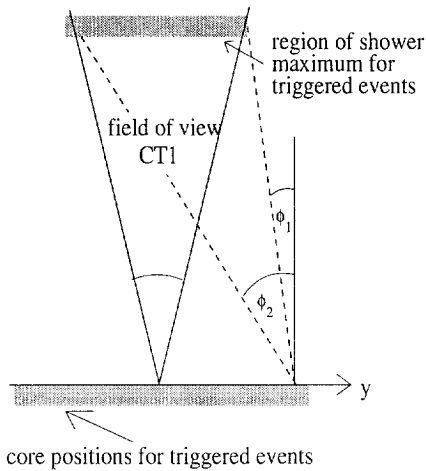
Fig. 14. Schematic drawing to illustrate the correlation between shower angle and shower core. Not drawn to scale.
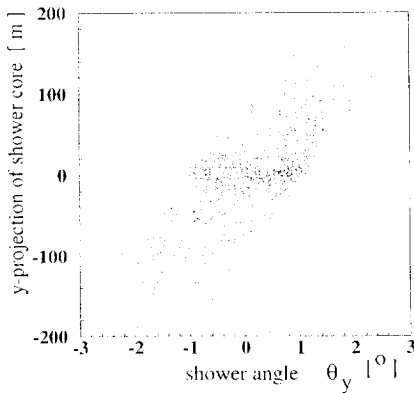

Fig. 15. The y-projection of the shower core vs. the y-projection of the shower angle. A shower angle $\theta_y = 0$ implies a shower parallel to the telescope axes; the telescope position is $y = 0$.

7. Timing information

Two 12-bit LeCroy 2228 TDCs with 250 ps/channel resolution are used to register the arrival time difference of the Cherenkov light front hitting the telescopes. The start signal is the trigger of one telescope, the stop signal is the delayed trigger signal of the other telescope. The information of the second TDC is thus redundant. For a shower parallel to the telescope axis the time difference between the start and stop signal depends on the actual separation d_{12} of the image planes (see Fig. 1(a)). A shower with an inclination θ_x relative to the telescope axis leads to
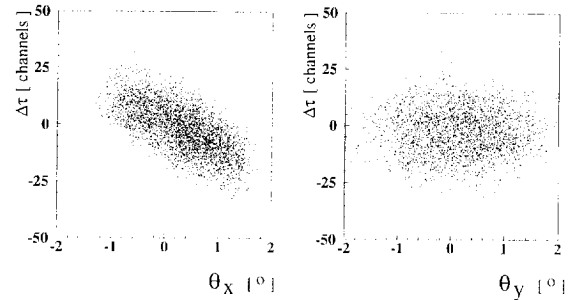

Fig. 16. $\Delta\tau$, the deviation of the TDC value from the mean value, vs. the x- and y-projection of the reconstructed shower angle.

an additional time difference

$$\Delta\tau \approx \frac{L_m\theta_x}{c}$$

with L_m as the telescope distance projected into the camera plane. The deviation $\Delta\tau$ of the TDC value from its mean value for the actual hour angle is a measure of θ_x.

Fig. 16 shows the correlation between the shower angles reconstructed from the images and the TDC result. There is a good correlation of $\Delta\tau$ with θ_x, featuring the correct slope, whereas θ_y and $\Delta\tau$ are uncorrelated. This result provides a consistency check of the reconstruction technique. However, the width of the $\Delta\tau$ vs. θ_x distribution provides only an upper limit of 0.5° for the precision of the reconstruction. The timing measurement contributes significantly to the width of this distribution, in particular since the location of the two measurement locations on the Cherenkov cone is a priori unknown, introducing errors up to the size of the cone slope, which is about 1°.

8. Resolution in the image and shower parameters

Two methods were studied to estimate the achievable resolution in the shower parameters: one can either rely on Monte Carlo simulations, or one can use the redundant information of stereoscopic images to experimentally determine the resolution of the image parameters, such as the image center of gravity or the orientation of the image, with the option to propagate these errors into errors of derived parameters like the shower direction.

The resolution of the image centers can be derived from the data using the image center correlations (as-

Determination of the image center resolution along the minor axis
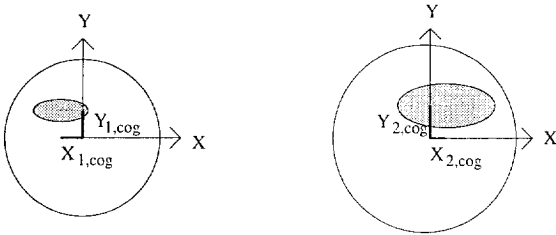
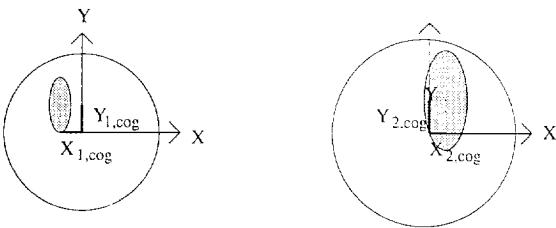Determination of the image center resolution along the major axis

Fig. 17. Determination of the resolution of the image center using the image center correlation. The width of the $y_{2,cog} - y_{1,cog}$-distribution measures the resolution along the minor axis in the top figure and along the major axis in the bottom figure.

suming that the resolution is the same for both telescopes). The width of the $y_{2,cog} - y_{1,cog}$ distribution (Fig. 5(b)) is then given by $\sqrt{2}$ times the image center resolution. The rms-width of $x_{2,cog} - x_{1,cog}$ distribution (Fig. 5(a)) is slightly larger (by 15–20%); this is expected since in this projection the fluctuations in shower height also contribute (Fig. 6). The resolution of the image centers can be determined along the major and minor axis of the image separately by using events with both images oriented along the x- and y-axis, respectively (Fig. 17). To provide enough statistics, events with an angle $\leq 5°$ to the relevant axis were used. One obtains a resolution of $0.13°$ (equivalent to 0.3 times the pixel size) along the major axis and $0.06°$ (equivalent to 0.13 pixels) along the minor axis.

Events with a core location on or near the x-axis can be used to obtain a coarse estimate of the resolution $\Delta\alpha$ in the angular orientation of the images. One uses a first telescope to 'tag' such events (where the image points to the location of the other telescope), and looks at the orientation of the second image, which shows a peak in the direction of the 'tagging' telescope, superimposed on a background caused by events in the

direct vicinity of the second telescope. The resulting resolutions in the range of $10°$ to $15°$ agree with the more precise values of $14 \pm 1°$ (CT1) and $11 \pm 1°$ (CT2) obtained from the full Monte Carlo simulations described below.

The resolution of the shower direction and core position was determined with Monte Carlo simulations of gamma- and proton-induced showers, using the same reconstruction procedure as in the data. Table 2 summarizes the results. The errors quoted were derived by fitting a gaussian distribution, superimposed on a flat background, to the $p = p_{rec} - p_{true}$ distribution of the difference between the true and reconstructed parameter p. The uniform background, particularly relevant in the measurement of core positions, results from poorly reconstructed events, e.g. events close to the camera edge, and from events where the two image center lines intersect under small angles.

One can see that the errors on gamma shower parameters are on average significantly smaller than those of proton showers. This is mostly due to the fact that gamma showers have more compact images than proton showers. The mean directional error $\Delta\theta = \sqrt{(\Delta\theta_x)^2 + (\Delta\theta_y)^2}$ is about $0.26°$ for gammas and $0.5°$ for protons.

9. Analysis of Crab Nebula data

As a final check of the stereoscopic analysis procedure, 10^5 events from simultaneous Crab Nebula observations from September to December 1994 were analyzed. The data comprise about 40 h of observation made up of 20 minute ON-source/20 minute OFF-source scans. The data were checked for correct tracking and other hardware problems. Runs with low coincidence rates due to poor weather conditions as well as run pairs with a raw coincidence signal of more than 3.5 σ were excluded. Of a total of 123 ON–OFF pairs, 71 were accepted.

To calculate the Hillas parameters, image pixels were selected as described previously, requiring either that a pixel be well above the noise, or has a 'good' neighbor pixel. During the Crab observations, the bright star ζ Tauri is in the field of view of the camera, about $1.1°$ from the telescope axis. The pixel containing ζ Tauri was set to zero both in the ON- and in the OFF-runs. To reject poor images, only events

Table 2
The resolution in the x and y components of the core position and of the shower angle, for gamma showers in two energy ranges and for protons following a cosmic ray energy spectrum, as derived from Monte Carlo shower simulations. The numbers in parentheses give the ratio of the amplitude of the gaussian peak to the uniform background

	p	γ 2–3 TeV	γ 7–10 TeV
Δx_{core}	20.2 ± 1.4 m (3.2)	11.6 ± 1.7 m (10.2)	7.2 ± 1.0 m (12.6)
Δy_{core}	23.8 ± 1.5 m (3.5)	11.1 ± 1.5 m (9.4)	6.2 ± 1.3 m (8.7)
$\Delta\theta_x$	0.35 ± 0.01° (19.6)	0.17 ± 0.01° (62.4)	0.15 ± 0.01° (45.2)
$\Delta\theta_y$	0.33 ± 0.01° (31.4)	0.20 ± 0.02° (42.6)	0.22 ± 0.02° (30.2)

with 3 or more 'picture' pixels in each camera were processed. In this filtering step, the number of events was reduced from 54701 (ON) and 53579 (OFF) to 49834 (ON) and 48516 (OFF), respectively. As the pixel containing ζ Tauri is part of the hardware trigger, the number of ON-events is significantly (about 2.7% or 4.2 σ) larger than the number of OFF events. Within statistics, the excess is equally distributed throughout the run pairs. This excess in the raw data was artificially set to zero by scaling the OFF-distributions up by a factor 1.027. This procedure should be conservative, since the following cuts on showers pointing to the Crab nebula should anyway remove most of the excess triggers associated with ζ Tauri.

After calculating the Hillas parameters of the single images, the shower core position and shower angle of each event was determined. The reconstructed shower angle was used to search for a signal from the direction of the Crab. To suppress the hadron background, events were preselected using cuts on the image shape parameters *length, width,* and *concentration.* Note that these parameters depend only on the shape of the images, but not on their location within the cameras (apart from edge effects); it was deliberately tried to separate shape cuts (for the gamma/hadron separation) from pointing cuts as much as possible. The values of the cuts on length, width, and concentration were determined based on Monte Carlo simulations of gamma-induced showers; the cuts were chosen such that each provides 90% efficiency for gamma-induced showers, if applied individually. The optimum values for these cuts depend on the angle under which the shower is viewed, i.e., on the distance R between a telescope and the shower axis, and on the zenith angle. For vertical showers, width cuts, e.g., range from $0.25°$ ($R < 40$ m) to $0.16°$ ($R > 120$ m) for CT1,
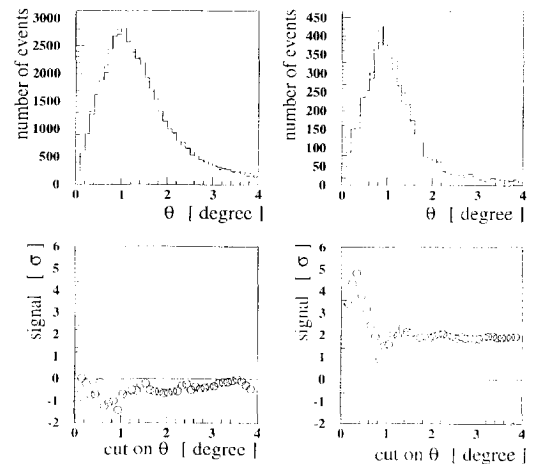

Fig. 18. The gamma signal from the Crab Nebula for the data set before (left side) and after (right side) hadron suppression. The top picture shows the ON- (solid line) and OFF- (dashed line) shower angle distributions, the bottom pictures show the obtained signal in units of standard deviations σ as a function of the cut on shower angle θ. After hadron suppression, one obtains a signal of more than 4 σ with a cut on showers with $\theta \leq 0.4°$.

and from $0.35°$ to $0.21°$ for CT2. After the stereoscopic reconstruction the distance to the shower axis is known (in contrast to a single telescope), and the appropriate cut values are chosen. If the intersection angle of the two lines used to determine the shower parameters is smaller than 25°, the determination of the core distance is quite uncertain. In such cases, cuts depending on *zone* (the pixel ring containing the image centroid) had to be applied. The validity of the cuts was checked by comparing image parameter distributions of Monte Carlo proton showers with the data, after simulating the hardware trigger and using the same software cuts and analysis procedure.

For each of the two telescopes in coincident events,

the three orientation-independent shape cuts are applied – *length, width,* and *concentration.* Events passing at least 5 of these 6 cuts form the gamma-enhanced dataset. Fig. 18 shows the distributions in the angle between the shower axis and the telescope axes, i.e., the direction to the Crab. For the full sample, before applying the shape cuts, the ON–OFF difference is slightly negative. This was to be expected, given that the OFF-distributions were conservatively scaled up by 2.7% in order to account for the higher ON-source trigger rates caused by ζ-tauri; in a stereoscopic reconstruction, ζ-tauri induced events are likely to reconstruct far from the telescope axis. In the gamma-enhanced sample, an excess is seen in the ON-sample for angles less than 0.4° from the source. After a cut of 0.4° on shower angle, a signal of more than 4 σ is obtained, with 138 excess events over a background of about 350 events, corresponding to a signal-to-noise ratio of about 0.4. This cut value is in reasonable agreement with the resolution in the projected angles for gamma showers, $\Delta\theta_{x,y} \approx 0.2°$, obtained from Monte Carlo simulations; the optimum significance should be obtained with a cut at $1.6\Delta\theta_{x,y}$.

The signal did not improve significantly if cuts on the quality of the images and the reconstruction were applied, by requiring, e.g., a minimum distance of images from the camera borders or a minimum stereo angle. This is not surprising, since in particular due to the small camera of CT1, any useful cut is accompanied by a drastic loss in event statistics. Also, errors in the reconstruction should not influence the level of the flat cosmic-ray background; they simply cause the loss of a few 'good' events, which then contribute to an almost negligible increase in the background level.

An interesting question is by how much the net performance of a telescope system is improved using the stereoscopic reconstruction technique, compared to an individual operation and analysis of each telescope. Based on the present analysis, it is however not possible to conclusively address this issue. For a given number of events, the stereoscopic reconstruction clearly provides increased significance of the Crab signal. However, under present conditions, the number of useful coincident events is small compared to the total number of events; the data obtained with the two HEGRA prototype telescopes suffer from the unequal properties of the telescopes (in particular, the small field of view of CT1). Furthermore, the sys-

tem does not yet make use of a hardware trigger coincidence between telescopes, which will allow to reduce the thresholds for the individual telescope triggers, and will enhance the rate of coincident events. Data from the future telescopes will provide the basis for a conclusive experimental determination of the improvement factor.

10. Conclusions

The techniques for the analysis and stereoscopic reconstruction of coincident events in IACTs are introduced, and applied to data from the first two HEGRA Cherenkov telescopes. The reconstruction procedure allows to determine the shower direction, the core location, and the height of the shower maximum. The events show the expected properties, which are interpreted in terms of simple geometrical considerations. Data are consistent with the expected angular resolution of about 0.26° for gamma ray showers, limited mainly by the coarse granularity of the prototype cameras.

References

[1] R. Mirzoyan et al., Nucl. Instrum. Methods. A 351 (1994) 51.
[2] A.M. Hillas, Proc. 19th Int. Cosmic Ray Conf. (La Jolla) 3 (1985) 445.
[3] D. Petry, Ph.D. Thesis, Munich, in preparation.
[4] P.T. Reynolds et al., Astrophys. J. 404 (1993) 206.
[5] F. Aharonian et al., J. Phys. G 21 (1995) 419.
[6] G. Vacanti et al., Astrophys. J. 377 (1991) 467.
[7] A. Konopelko et al., Astropart. Phys. 4 (1996) 199.